PCCP

PAPER

View Article Online
View Journal | View Issue

Cite this: *Phys. Chem. Chem. Phys.*, 2023, **25**, 4005

Quasi-classical trajectory study of the OH^- + CH_3I reaction: theory meets experiment†

Domonkos A. Tasi, *[a] Tim Michaelsen,[b] Roland Wester [b] and Gábor Czakó *[a]

Received 28th November 2022,
Accepted 16th December 2022

DOI: 10.1039/d2cp05553h

rsc.li/pccp

Regarding OH^- + CH_3I, several studies have focused on the dynamics of the reaction. Here, high-level quasi-classical trajectory simulations are carried out at four different collision energies on our recently developed potential energy surface. In all, more than half a million trajectories are performed, and for the first time, the detailed quasi-classical trajectory results are compared with the reanalysed crossed-beam ion imaging experiments. Concerning the previously reported direct dynamics study of OH^- + CH_3I, a better agreement can be obtained between the revised experiment and our novel theoretical results. Furthermore, in the present work, the benchmark geometries, frequencies and relative energies of the stationary points are also determined for the OH^- + CH_3I proton-abstraction channel along with the earlier characterized S_N2 channel.

I. Introduction

Moving further to larger systems, the investigations of bimolecular nucleophilic substitutions (S_N2) have become more and more complex over the last few decades.[1–9] The most thoroughly studied seven-atomic S_N2 reactions are OH^- + CH_3Y (Y = F, Cl, Br, I). In these cases, the S_N2 reaction profile differs from the traditional $X^-\cdots CH_3Y \rightarrow [X\cdots CH_3\cdots Y]^- \rightarrow XCH_3\cdots Y^-$ path.[10–15] For Y = Cl, Br and I, in the entrance channel, a H-bonded $HO^-\cdots HCH_2Y$ complex and a H-bonded transition state are located, and for Y = I, the typical $X^-\cdots CH_3Y$ ion-dipole pre-reaction complex and the $[X\cdots CH_3\cdots Y]^-$ Walden-inversion transition state cannot be found. Moreover, instead of the $XCH_3\cdots Y^-$ post-reaction complex, a H-bonded $CH_3OH\cdots Y^-$ complex is situated in the product channel, which happens to be the global minimum for the OH^- + CH_3Y reactions. It should be noted that, by front-side attack[16] and double-inversion[17] mechanisms, retention of the initial configuration may also occur in the OH^- + CH_3Y S_N2 reaction.[15]

In 2002, Hase and co-workers investigated the reaction between OH^- and CH_3F using direct dynamics classical trajectory simulations, and revealed that the reaction rather takes place through a direct route by avoiding the deep $CH_3OH\cdots F^-$ well in the exit channel.[12] The stationary points of the OH^- + CH_3F Walden-inversion pathway were characterized by Sun *et al.*[13] at HF, MP2 and CCSD(T) levels of theory and by Gonzales *et al.*[18,19] using density functional theory and the focal-point approach. Recently, based on the results of Hase and co-workers, several reaction analysis methods were applied for the reaction of OH^- and CH_3F.[20–24] Furthermore, dynamics simulations uncovered a novel oxide ion substitution for the reaction: in the post-reaction $CH_3OH\cdots F^-$ complex the leaving F^- may remove the proton of the hydroxyl group, which leads to the products of HF + CH_3O^-.[25,26] The existence of the oxide ion substitution for OH^- + CH_3F was also confirmed by Li and co-workers,[27] and Ji *et al.* completed a detailed mapping of the possible proton abstraction-involved channels for the $Y^-(H_2O)_n$ + CH_3I (Y = F, Cl, Br, I) reactions, where n = 1 or 2, taking into account an oxide ion substitution leading to the CH_3O^- + HY + HI + $(n-1)H_2O$ products.[28] The OH^- + CH_3Cl S_N2 reaction was examined by various studies as well. The stationary points were identified by Evanseck *et al.*,[10] and later the results were recalculated by Tachikawa *et al.*,[11] Souza *et al.*,[29] Laloo *et al.*[30] and Zhao *et al.*[31] using DFT, HF, MP2 and CCSD(T) methods; moreover, direct dynamics simulations were also conducted at the HF/3-21+G(d) and B3LYP/aug-cc-pVDZ levels of theory.[31,32] Wang and co-workers performed QM/MM calculations for the OH^- + CH_3Y (Y = F, Cl and Br) S_N2 reactions in aqueous solution.[33–35]

For the OH^- + CH_3I reaction, numerous experimental and theoretical investigations were carried out in the last

[a] *Interdisciplinary Excellence Centre and Department of Physical Chemistry and Materials Science, Institute of Chemistry, University of Szeged, Rerrich Béla tér 1, Szeged H-6720, Hungary. E-mail: dtasi@chem.u-szeged.hu, gczako@chem.u-szeged.hu*

[b] *Institut für Ionenphysik und Angewandte Physik, Universität Innsbruck, Technikerstraße 25/3, 6020 Innsbruck, Austria*

† Electronic supplementary information (ESI) available: Integral cross sections ($bohr^2$) of the possible pathways, structures of the stationary points for the S_N2 and proton-abstraction pathways with the most important bond lengths (Å) and angles (deg) obtained on the PES compared to the CCSD(T)-F12b/aug-cc-pVTZ values, opacity functions of the S_N2 and proton-abstraction pathways, Cartesian coordinates (Å) and energies (E_h) of the stationary points for the proton-abstraction channel obtained at the CCSD(T)-F12b/aug-cc-pVTZ level of theory. See DOI: https://doi.org/10.1039/d2cp05553h

decade.[14,36–43] Cross-beam imaging techniques were employed to analyse the dynamics of the reactions of OH^-, $OH^-(H_2O)$ and $OH^-(H_2O)_2$ with CH_3I at collision energies (E_{coll}) of 11.5, 23.1, 34.6 and 46.1 kcal mol^{-1}.[37] Considering the I^- velocity vector distributions, three different S_N2 reaction mechanisms were observed, and their occurrences were dependent on the presence of the water molecules. The stationary points of the latter reactions were studied, as well, using DFT and MP2 methods.[14,38,39,41] The crossed-beam and selected ion flow tube experiments were supported by the direct dynamics simulations of Hase and co-workers in order to describe the dynamics and kinetics of the reaction.[14,38,40,42] These findings, along with others, showed that the dynamics of the S_N2 reactions had to be rethought, because the picture is more complex than the traditional one.[44] For that reason, in 2018, we characterized the Walden-inversion, front-side attack and double-inversion mechanisms of the $OH^- + CH_3Y$ (Y = F, Cl, Br, I) S_N2 reactions with high-level *ab initio* methods.[15] In 2020, for the title reaction, several global analytical potential energy surfaces (PESs) were developed utilizing the in-house Robosurfer program package.[45,46] The final choice of the *ab initio* method was not evident: quasi-classical trajectory (QCT) simulations on the PESs unveiled that the gold-standard CCSD(T) method provides unphysically negative energies at some regions of the PES, and therefore a composite *ab initio* method was applied to obtain the energies of the structures.

In this work, we report a more detailed dynamical study of the $OH^- + CH_3I$ reaction. At first, for the title reaction, we determine the benchmark geometries, frequencies and energies of the stationary points of the proton-abstraction pathway using the modern explicitly correlated CCSD(T)-F12b method in order to explore the energetics of the competing S_N2 and proton-abstraction channels. Then, utilizing our previously constructed PES,[45] in total more than half a million QCT computations are run at E_{coll} of 11.5, 23.1, 34.6 and 46.1 kcal mol^{-1} providing the integral cross-sections (ICSs) of the possible reaction mechanisms, the scattering angle distributions and the translational and internal energy distributions of the S_N2 and proton-abstraction products, as well. Last but not least, the QCT results are compared with the reanalysed crossed-beam imaging experiments for the $OH^- + CH_3I$ reaction. The details of the theoretical and experimental methods are given in Section II. The results are described and discussed in Section III, and in Section IV, the summary of the work can be found.

II. Computational and experimental methods

For the *ab initio* characterization of the $OH^- + CH_3I \rightarrow H_2O + CH_2I^-$ reaction, the same process is implemented as for the S_N2 channel discussed in ref. 15: the stationary points are searched at the MP2/aug-cc-pVDZ level of theory,[47] then, for the more accurate energies, structures and frequencies, the modern explicitly correlated coupled cluster singles, doubles and perturbative triples CCSD(T)-F12b method[48] is employed with the correlation-consistent aug-cc-pVDZ and aug-cc-pVTZ basis sets.[49] The benchmark classical energies are obtained utilizing the CCSD(T)-F12b method with the aug-cc-pVQZ basis set at the CCSD(T)-F12b/aug-cc-pVTZ geometries, and considering the post-CCSD(T) correlation effects[50–52] and the core correlation corrections. Taking account of the zero-point energy (ZPE) of the corresponding stationary point, the adiabatic energy is determined. For I, a small-core relativistic effective core potential[53] is applied with the aug-cc-pV*n*Z-PP (n = 2, 3, 4) and aug-cc-pwCVTZ-PP basis sets. Most of the *ab initio* calculations are performed using the Molpro program package,[54] except for CCSDT and CCSDT(Q) where the MRCC program is used.[55,56] A more detailed description of the *ab initio* computations is given in ref. 15.

On our previously developed PES, QCT simulations are carried out for the reaction of $OH^- + CH_3I$ at 11.5, 23.1, 34.6 and 46.1 kcal mol^{-1} E_{coll}. In ref. 45, the interested reader may find the details about the PES development. It should be noted that the energy points of the PES are computed at the CCSD-F12b/aug-cc-pVTZ + BCCD(T)/aug-cc-pVDZ − BCCD/aug-cc-pVDZ composite level of theory[57] to resolve the failure of the CCSD(T)-F12b method. With regard to the conditions of the simulations, the vibrational ground states of the reactants (v = 0) are prepared by normal-mode sampling,[58,59] and the rotational angular momenta are set to zero. The initial orientations of the reactants are randomly sampled, and the initial distance of OH^- and CH_3I is 40 bohr with a given impact parameter (b). At each b, 5000 trajectories are propagated and b is scanned from 0 to b_{max} (where the probability of the reaction becomes 0) with a step size of 0.5 bohr. Each trajectory is run with a time step of 0.0726 fs until the largest interatomic distance becomes larger by 1 bohr than the largest initial one. The opacity function ($P(b)$) is defined by the reaction probability as a function of b. At each E_{coll}, the ICS of each reaction channel is determined by a b-weighted numerical integration of the corresponding $P(b)$:

$$\mathrm{ICS} = 2\pi \int_0^{b_{max}} P(b) b \mathrm{d}b \quad (1)$$

which is expressed by the trapezoidal rule of the numerical integration. The scattering angle (θ) is the angle of the relative velocity vectors of the centre of masses of the OH^- and CH_3I reactants and the relevant products. The distributions of θ are attained by binning the cosine of the θ into 10 (for S_N2) and 20 (for proton abstraction) equidistant bins from −1 to 1, where $\cos(\theta)$ = 1 corresponds to forward scattering. For the ICS of proton abstraction, two types of ZPE constraints are applied: (1) soft: reject trajectory if the sum of the classical vibrational energies of the CH_2I^- and H_2O products is smaller than the sum of their ZPEs on the PES, (2) hard: reject trajectory if the vibrational energy of either product is less than its ZPE on the PES. The product channels of the $OH^- + CH_3I$ reaction are differentiated by determining the relevant bond distances of the corresponding products similarly as for the case of $NH_2^- + CH_3I$.[60] Note that, the distinction of the four different channels of

proton abstraction with dissociation is based on the different C–I, O–I and C–O distances.

The experimental data on the OH^- + CH_3I reaction have been obtained using crossed-beam velocity map imaging, as described in earlier publications.[14,36,37] In brief, the negative ions were produced in a pulsed plasma discharge, mass-selected by time-of-flight, and stored in an octupole ion trap at about 100 K to cool the translational and rotational motion. After extraction from the trap, the ions were crossed with a supersonic neutral jet of CH_3I seeded in helium with relative collision energies selected between 11.5 and 46.1 kcal mol^{-1} (0.5 and 2.0 eV). Product ions were mapped by a velocity map imaging spectrometer onto a position- and time-sensitive detector and for each reactive event the detector information was transformed into a product mass and velocity vector in the centre-of-mass frame. From the three-dimensional velocity distribution, the angular and internal energy distributions are integrated after multiplication with an appropriate Jacobian. During re-evaluation of the data, we noticed that for the integration of the relative translational energy distributions shown in Fig. 6 of ref. 14, an incorrect Jacobian was used, which is corrected in the present work.

III. Results and discussion

The stationary points of S_N2 and proton-abstraction channels of the OH^- + CH_3I reaction are shown in Fig. 1 with the corresponding benchmark classical relative energies and PES values. The detailed *ab initio* energies are summarized in Table 1 and the structures of the stationary points are given in Fig. S1 (ESI†). Similar to the back-side attack Walden-inversion (HMIN → HTS → PostHMIN), proton abstraction is also a submerged pathway, although S_N2 is much more exothermic with a reaction energy of 66.64 kcal mol^{-1}. In the entrance

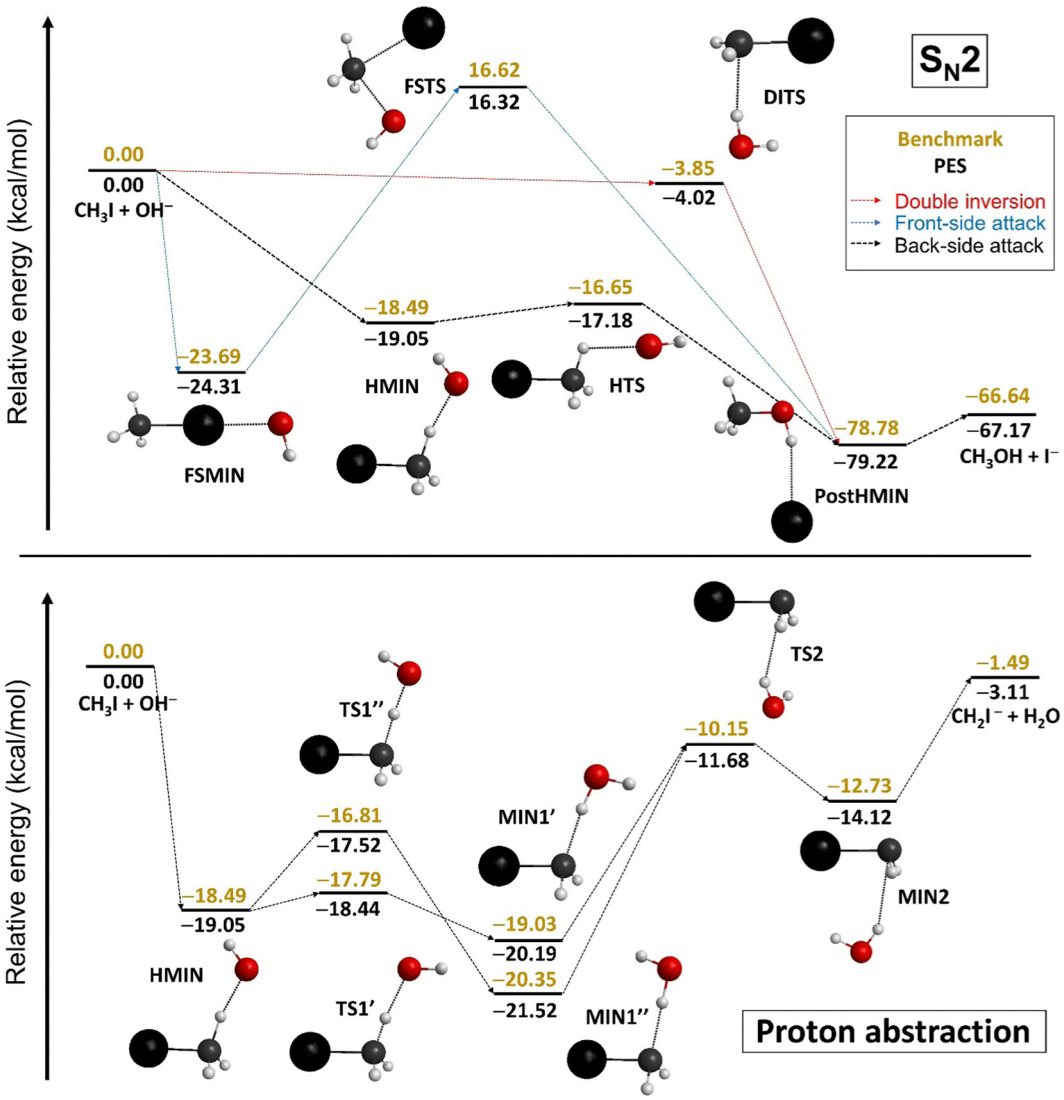

Fig. 1 The schematic potential energy surfaces of the S_N2 and proton-abstraction pathways for the OH^- + CH_3I reaction showing the classical benchmark relative energies (kcal mol^{-1}) of the stationary points with the corresponding PES values, relative to OH^-(eq.) + CH_3I(eq.). In the case of the S_N2 channel, the benchmark energies and PES values are derived from ref. 15 and 45, respectively.

Table 1 Benchmark classical and adiabatic energies (kcal mol^{-1}) of the stationary points, relative to the OH^-(eq.) + CH_3I(eq.) reactants, for the S_N2 and proton-abstraction pathways of the OH^- + CH_3I reaction. For the OH^- + CH_3I S_N2 reaction, the benchmark classical and adiabatic *ab initio* energies are adapted from ref. 15

S_N2	DZ[a]	TZ[b]	QZ[c]	δT[d]	δ(Q)[e]	Δcore[f]	Classical[g]	ΔZPE[h]	Adiabatic[i]
HMIN	−18.89	−18.64	−18.48	−0.02	0.00	0.02	−18.49	0.42	−18.07
HTS	−16.74	−16.69	−16.57	−0.04	−0.04	0.01	−16.65	0.50	−16.15
PostHMIN	−79.30	−79.08	−79.43	0.09	0.27	0.29	−78.78	4.49	−74.29
FSMIN	−24.09	−24.10	−24.05	0.07	−0.23	0.51	−23.69	0.68	−23.01
FSTS	17.19	17.03	17.10	−0.11	−0.79	0.42	16.62	0.58	17.20
DITS	−4.20	−4.13	−4.05	0.07	−0.01	0.15	−3.85	0.18	−3.67
I^- + CH_3OH	−67.16	−67.08	−67.71	0.08	0.31	0.67	−66.64	3.98	−62.67
ABS	**DZ[a]**	**TZ[b]**	**QZ[c]**	**δT[d]**	**δ(Q)[e]**	**Δcore[f]**	**Classical[g]**	**ΔZPE[h]**	**Adiabatic[i]**
TS1′	−18.19	−17.92	−17.76	−0.04	−0.02	0.02	−17.79	0.33	−17.45
TS1″	−17.38	−17.11	−16.93	0.01	−0.02	0.14	−16.81	−1.93	−18.74
MIN1′	−19.60	−19.49	−19.36	−0.02	0.04	0.32	−19.03	0.33	−18.70
MIN1″	−20.89	−20.80	−20.69	−0.03	0.04	0.32	−20.35	0.53	−19.82
TS2	−10.65	−10.60	−10.57	−0.06	0.06	0.41	−10.15	−0.08	−10.23
MIN2	−13.14	−13.13	−13.07	−0.06	0.05	0.35	−12.73	0.56	−12.16
CH_2I^- + H_2O	−1.77	−1.96	−2.08	−0.07	0.11	0.56	−1.49	−1.33	−2.82

[a] CCSD(T)-F12b/aug-cc-pVDZ. [b] CCSD(T)-F12b/aug-cc-pVTZ. [c] CCSD(T)-F12b/aug-cc-pVQZ. [d] CCSDT/aug-cc-pVDZ − CCSD(T)/aug-cc-pVDZ. [e] CCSDT(Q)/aug-cc-pVDZ − CCSDT/aug-cc-pVDZ. [f] AE-CCSD(T)/aug-cc-pwCVTZ − FC-CCSD(T)/aug-cc-pwCVTZ. [g] QZ + δT + δ(Q) + Δcore. [h] ΔZPE(CCSD(T)-F12b/aug-cc-pVTZ). [i] QZ + δT + δ(Q) + Δcore + ΔZPE.

channel of S_N2 the Y···OH^--bonded front-side complex is below HMIN and the global minimum of the reaction is in the product channel of S_N2 (PostHMIN) with a classical energy of −78.78 kcal mol^{-1}. In the case of proton abstraction, involving the same H-bonded complex (HMIN) in the reactant channel as for S_N2, four minima and three transition states can be found: HMIN → TS1′/TS1″ → MIN1′/MIN1″ → TS2 → MIN2. As it can be seen in Fig. 1 and Fig. S1 (ESI†), TS1′ and TS1″, as well as, MIN1′ and MIN1″ are conformational isomers, due to the torsional motion of OH^-: For TS1′ and MIN1′, the torsion angle of I–C···O–H^- is 180° (*trans* arrangement), while for TS1″ and MIN1″ the value is 0° (*cis* arrangement). The energies of the isomers are similar, TS1′ is below TS1″ by 0.98 kcal mol^{-1} and MIN1′ is above MIN1″ by 1.32 kcal mol^{-1}, without ZPE corrections (Fig. 1). It should be emphasised that, considering ZPE effects, an energy of −17.45 and −18.74 kcal mol^{-1} can be observed for TS1′ and TS1″, respectively, and since the benchmark adiabatic energy is −18.07 kcal mol^{-1} for HMIN, the barrier of TS1″ vanishes (Table 1). For the stationary points of proton abstraction, the post-CCSD(T) effects are small, whereas, for S_N2, more significant post-CCSD(T) effect can be determined, especially for FSTS (−0.90 kcal mol^{-1}). Generally, the post-CCSD(T) and the core correlation effects cancel each other, however, in some cases, accumulation of the effects still appears with the highest values of 1.06 and 0.60 kcal mol^{-1} for the S_N2 and proton-abstraction products, in order. The ZPE effects are usually between ±0.7 kcal mol^{-1}, except for PostHMIN, TS1″, I^- + CH_3OH and CH_2I^- + H_2O, where much higher effects occur: 4.49, −1.93, 3.98 and −1.33 kcal mol^{-1}, respectively. The DFT energies of the stationary points provided by Xie *et al.*[38] are in a qualitative agreement with our benchmark results, although the energy differences for several cases are larger than 2 kcal mol^{-1}, especially for TS1″, showing a deviation of −2.96 kcal mol^{-1}. This latter energy discrepancy shows that by employing DFT method, TS1″ happens to be below TS1′, and the barrier heights of TS1″ and TS1′ remarkably diminish (0.30 and 0.44 kcal mol^{-1}) compared to the benchmark classical values (1.68 and 0.70 kcal mol^{-1}, in order). As seen in Fig. 1, for the S_N2 pathway, the PES reproduces the benchmark energies of the stationary points within the chemical accuracy (±1 kcal mol^{-1}), while in the case of proton abstraction, PES provides slightly lower relative energies for MIN1′, MIN1″, TS2,

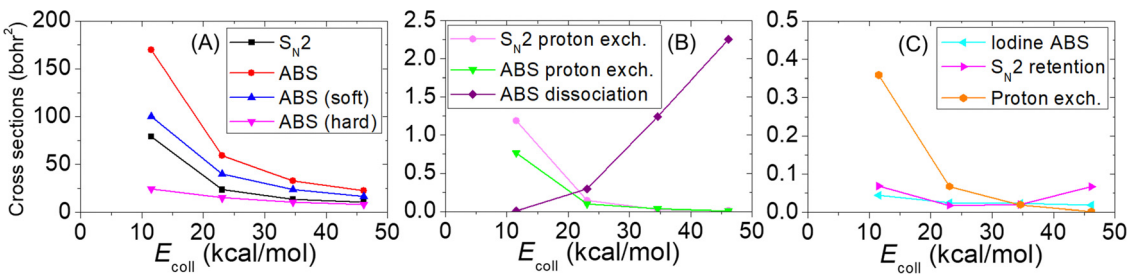

Fig. 2 Integral cross-sections for (A) S_N2, proton abstraction with soft and hard restriction; (B) S_N2 with proton exchange, proton abstraction with proton exchange and proton abstraction with dissociation; and (C) iodine abstraction, S_N2 with retention and proton exchange pathways of the OH^- + CH_3I reaction as a function of collision energy.

MIN2 and CH_2I^- + H_2O than the corresponding benchmark values, with differences of 1.16, 1.17, 1.53, 1.39 and 1.62 kcal mol^{-1}, respectively.

In order to characterize the dynamics of the title reaction, QCT computations are carried out at several E_{coll} (11.5, 23.1, 34.6 and 46.1 kcal mol^{-1}) on our earlier constructed analytical PES[45] (see Computational and experimental methods). The ICSs of the possible reaction channels at each E_{coll} are presented in Fig. 2 and in Table S1 (ESI†). As it is expected for barrierless reactions, with increasing E_{coll}, the ICSs of proton abstraction and S_N2 are decreasing. The largest ICSs are obtained for proton abstraction at each E_{coll}, peaking at a value of 169.8 $bohr^2$ at E_{coll} = 11.5 kcal mol^{-1}, and even with soft ZPE restriction, the ICSs of proton abstraction are larger than the corresponding values of the S_N2 channel. Using hard ZPE restriction for proton abstraction, the reaction probability suffers a significant decrease, as its ICSs are 23.9 and 14.8 $bohr^2$ at E_{coll} = 11.5 and 23.1 kcal mol^{-1}, respectively, while in the case of soft ZPE restriction, ICSs of 100.0 and 40.1 $bohr^2$ are determined. For S_N2, no ZPE violation can be obtained. The opacity functions of S_N2 and proton abstraction are shown in Fig. S2 (ESI†). Since the four hydrogen atoms can be distinguished during the course of a simulation, two additional pathways can be identified within S_N2: besides inversion, retention of the initial CH_3I configuration can also take place (S_N2 with retention), on the other hand, a proton exchange is feasible between the OH^- and CH_3I reactants followed by the traditional Walden inversion (S_N2 with proton exchange). Within proton abstraction, two other paths can be separated as well: following proton abstraction, a dissociation of the C–I bond may occur (proton abstraction with dissociation), and analogously to S_N2 with proton exchange, proton abstraction with proton exchange can proceed. Likewise for the NH_2^- + CH_3I reaction,[60] the formation of the products of iodine abstraction ($[I\cdots OH]^-$ + CH_3) is viable, although with a significantly lower probability, and in some cases, as for OH^- + CH_3F,[26] proton exchange between OH^- and CH_3I may eventuate resulting products apparently similar to reactants: OH^- + $CH_2H'I$ → HOH' + CH_2I^- → OH'^- + CH_2HI. Regarding the channels involving proton exchange, at lower E_{coll}, their ICSs are in the range of 0.3–1.2 $bohr^2$, whereas, at higher E_{coll}, these paths are almost negligible. Fig. 3 shows that proton abstraction with dissociation can be separated into four different channels with the largest probability of the CH_2 + I^- + H_2O product formation.

Performing crossed-beam ion imaging experiments for the OH^- + CH_3I reaction, the following product ions are detected: I^-, CH_2I^- and $[I\cdots H_2O]^-/[I\cdots OH]^-$. The latter product ions cannot be resolved individually, because the masses of the ions are almost equivalent (145 u/144 u), thus the time-of-flight peaks of $[I\cdots H_2O]^-$ and $[I\cdots OH]^-$ overlap. The experimental and theoretical branching ratios of these ions are shown in Table 2 at E_{coll} = 11.5, 23.1 34.6 and 46.1 kcal mol^{-1}. In QCT simulations, I^- is provided by three different reaction channels: S_N2 (I^- + CH_3OH) and two pathway-types of proton abstraction with dissociation (CH_2 + I^- + H_2O and I^- + $[CH_2\cdots H_2O]$). CH_2I^- is formed as a result of proton abstraction, and note that, for the branching ratios, the soft ZPE-restricted proton abstraction is taken into account. The product of $[I\cdots H_2O]^-$ is generated by one of the pathways of proton abstraction with dissociation, while $[I\cdots OH]^-$ occurs as a result of iodine abstraction, as seen in Fig. 2 and 3. At 11.5 kcal mol^{-1} E_{coll}, experiment assesses a slightly higher ratio for I^- than theory with a difference of ~1.4%, while at E_{coll} = 23.1 kcal mol^{-1}, a reversed situation appears, the formation of the I^- is overestimated by theory emerging a ~4.3% deviation. As a consequence, at low E_{coll}, the computed and measured ratios of the CH_2I^- product ion also differ from each other. Nevertheless, the agreement between theory and experiment is still impressive, almost quantitative, at these low collision energies. Furthermore, at higher E_{coll}, an excellent, clearly quantitative, agreement can be identified between the experimental and theoretical branching ratios of I^- and CH_2I^-: the differences of the corresponding ratios are below ~0.4%. At each E_{coll}, experiment reveals a more significant prevalence of the $[I\cdots H_2O]^-/[I\cdots OH]^-$ product ions, for instance at 46.1 kcal mol^{-1} E_{coll}, a value of 2.58% is measured,

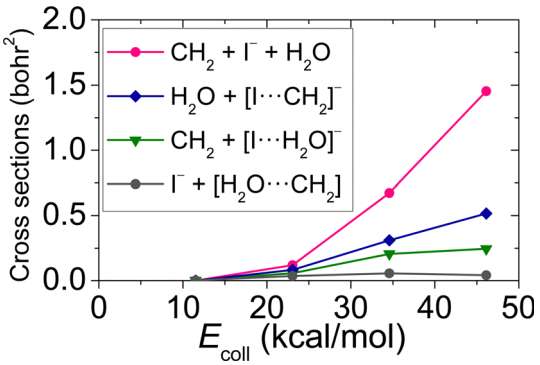

Fig. 3 Integral cross-sections for the different types of the proton abstraction with dissociation pathway of the OH^- + CH_3I reaction as a function of collision energy.

Table 2 The experimental and theoretical branching ratios (%) of the product anions of I^-, CH_2I^- and $[I\cdots H_2O]^-/[I\cdots OH]^-$ for the OH^- + CH_3I reaction at different collision energies. Note that for the theoretical branching ratios, soft ZPE-restricted proton abstraction is considered[a]

	I^-		CH_2I^-		$[I\cdots H_2O]^-/[I\cdots OH]^-$	
E_{coll} (kcal mol^{-1})	Exp.	Sim.[b]	Exp.	Sim.[c]	Exp.[d]	Sim.[e]
11.5	45.38	44.01	53.79	55.76	0.84	0.03
23.1	32.54	36.83	66.66	62.81	0.80	0.13
34.6	36.49	36.31	62.00	62.22	1.51	0.60
46.1	40.49	40.75	56.93	56.57	2.58	0.91

[a] 100% = ICS_{SN2} + $ICS_{ABS\ soft}$ + $ICS_{ABS\ dissociation}$ + $ICS_{Iodine\ ABS}$ + $ICS_{Proton\ exch.}$ [b] I^- originates from S_N2, and two channels of the proton abstraction with dissociation leading to CH_2 + I^- + H_2O or I^- + $[CH_2\cdots H_2O]$. [c] CH_2I^- originates from the soft-restricted proton abstraction. [d] The $[I\cdots H_2O]^-$ and $[I\cdots OH]^-$ ions cannot be distinguished from each other experimentally. [e] The sum of the branching ratios of the $[I\cdots H_2O]^-$ and $[I\cdots OH]^-$ product ions. $[I\cdots H_2O]^-$ originates from one of the channels of proton abstraction leading to the CH_2 + $[I\cdots H_2O]^-$ products, while $[I\cdots OH]^-$ is generated in iodine abstraction.

whilst theory provides only 0.91%. It should be highlighted that, in the case of proton abstraction with dissociation, QCT simulations unveil another product ion, $[I\cdots CH_2]^-$ (see Fig. 3), which may be detected by the crossed-beam technique as I^- if the complex dissociates during the time scale of the experiment or as CH_2I^- if the complex remains stable. Therefore, we do not consider the small fraction of $[I\cdots CH_2]^-$ (0%, 0.1%, 0.8% and 1.8% at E_{coll} = 11.5, 23.1 34.6 and 46.1 kcal mol^{-1}, respectively) at the branching ratio computations. Nonetheless, the direct dynamics simulations performed by Xie *et al.* gave branching ratios of 31%, 38% and 36%, for I^-, and 69%, 62% and 63% for CH_2I^- at E_{coll} = 11.5, 34.6 and 46.1 kcal mol^{-1}.[14]

For the products of OH^- + CH_3I S_N2 and the proton-abstraction reaction, the experimental and theoretical internal energy as well as scattering angle distributions are compared at several E_{coll} in Fig. 4 and 5. As we can distinguish the products of proton abstraction in each simulation, the internal energy contributions of CH_2I^- and H_2O can be determined, which is presented in Fig. 6. The theoretical translational energy distributions of the S_N2 and proton-abstraction products are shown in Fig. 7. In the case of the products of proton abstraction, with increasing E_{coll}, translational energies are more affected, than internal energies and the dominance of the forward-scattering becomes more and more favoured. These tendencies support a prevalence of the direct stripping mechanism at each E_{coll} for proton abstraction, and it should also be emphasised that experiment and theory are in accordance with each other. As it can

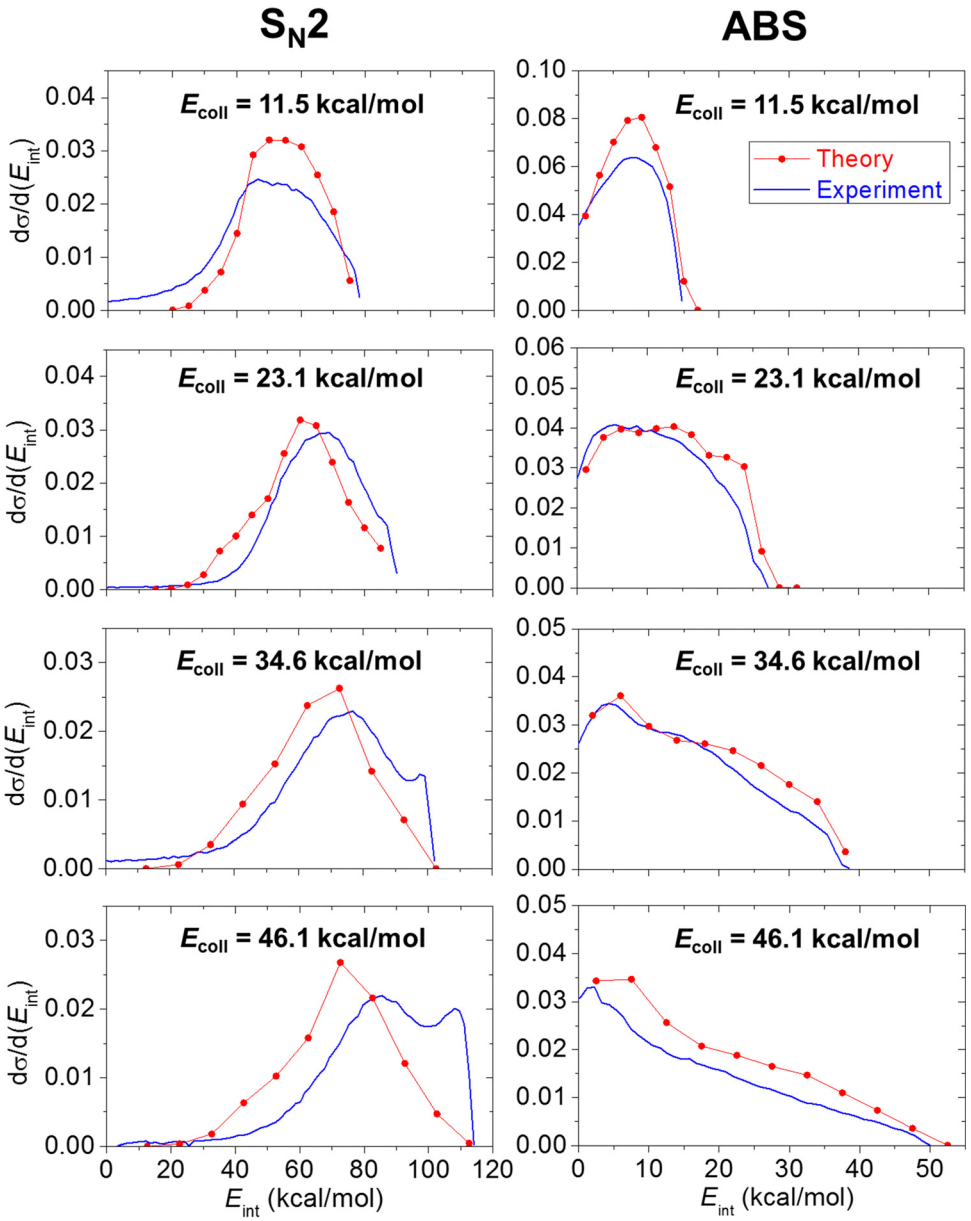

Fig. 4 Experimental and theoretical (ZPE-corrected) internal energy distributions of the products of the S_N2 (CH_3OH) and proton-abstraction (CH_2I^- + H_2O) channels of the OH^- + CH_3I reaction at different collision energies.

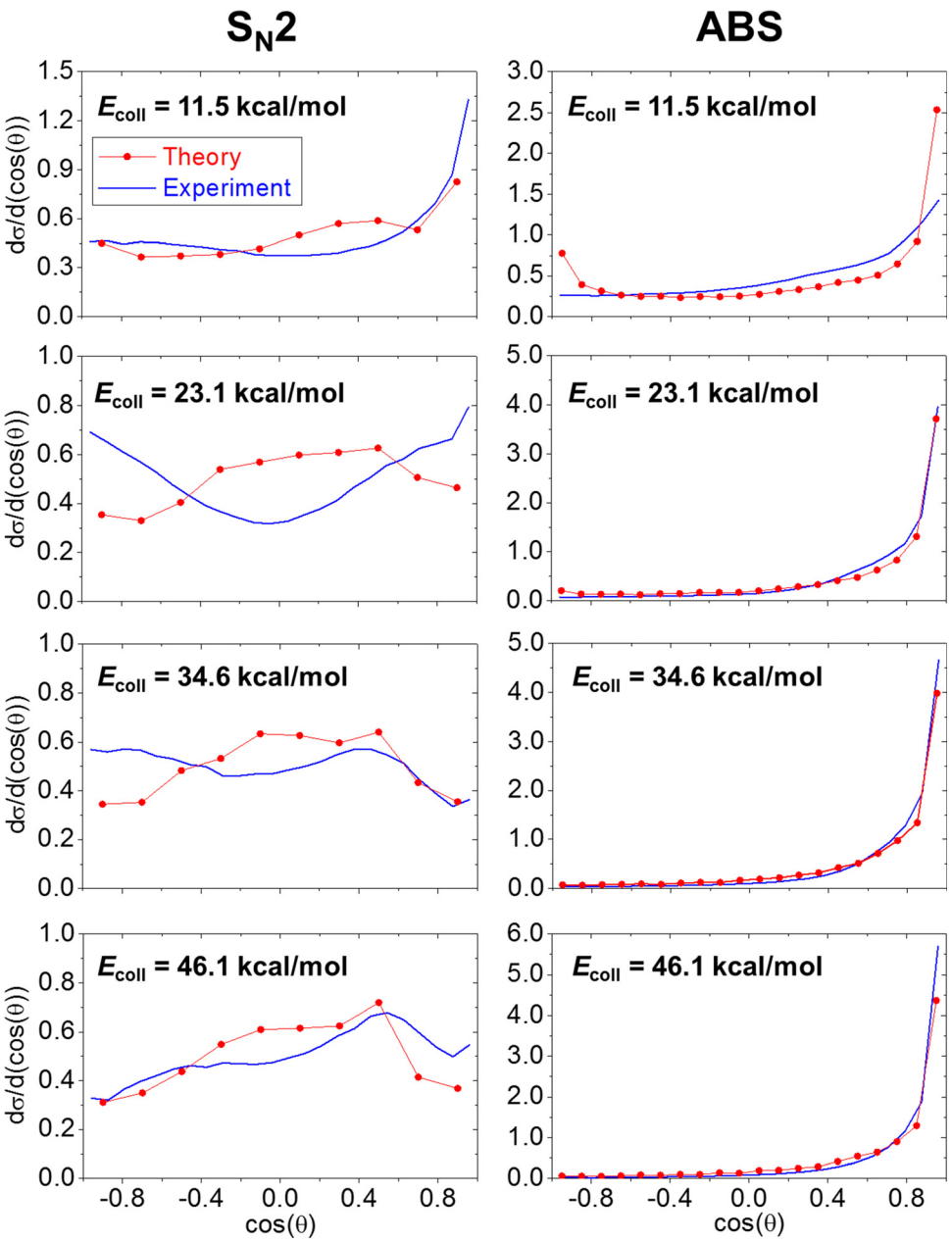

Fig. 5 Experimental and theoretical normalized scattering angle distributions of the products of the S_N2 (CH_3OH + I^-) and proton-abstraction (CH_2I^- + H_2O) channels of the OH^- + CH_3I reaction at different collision energies.

be expected, the internal energy contributions of the CH_2I^- product ion are more substantial than that of H_2O declaring that H_2O is more responsible for the hard-restricted proton-abstraction trajectories than CH_2I^-. In contrast, the dynamics of S_N2 has a different character: on the one hand, upon increasing E_{coll}, the CH_3OH internal energy is more impacted than translational energy showing an indirect feature. On the other hand, the scattering angle distributions of CH_3OH display forward and/or backward preference besides the isotropic character signifying direct stripping and/or rebound pathways as well as complex-forming indirect dynamics. As seen in Fig. 4 and 5, the experimental and theoretical CH_3OH internal energy distributions are in good agreement at E_{coll} = 11.5 and 23.1 kcal mol^{-1}, whilst theory underestimates internal energies at E_{coll} = 34.6 and 46.1 kcal mol^{-1}. Regarding the scattering angle distributions of the S_N2 products, a pleasant agreement can be identified, as well, except at E_{coll} of 23.1 kcal mol^{-1}, where experiment shows the preference of a dual forward-backward scattering; however computations reveal an isotropic feature. Concerning the direct dynamics computations of Xie *et al.*, for proton abstraction and S_N2, as well, a forward-scattered distribution is reported at E_{coll} = 11.5, 34.6 and 46.1 kcal mol^{-1}.[14]

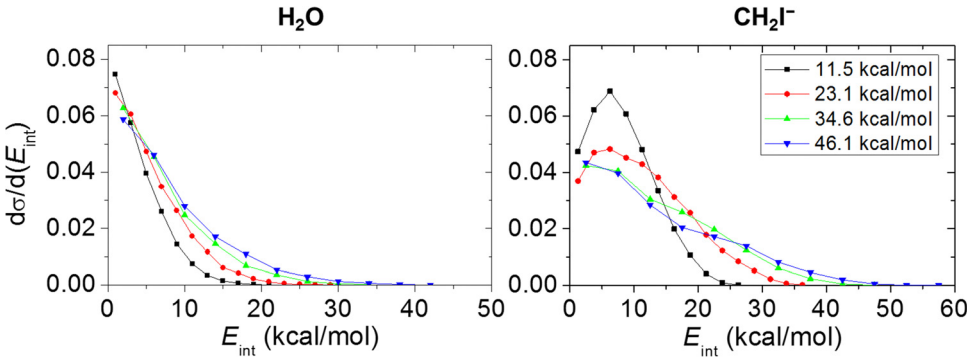

Fig. 6 Theoretical ZPE-corrected internal energy distributions of the products of the proton-abstraction channel (H_2O and CH_2I^-) of the OH^- + CH_3I reaction at different collision energies.

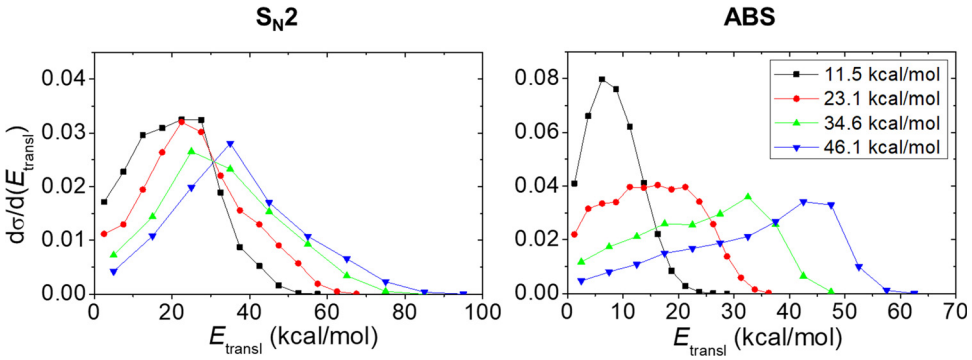

Fig. 7 Theoretical relative translational energy distributions of the products of the S_N2 (CH_3OH + I^-) and proton-abstraction (CH_2I^- + H_2O) channels of the OH^- + CH_3I reaction at different collision energies.

IV. Summary and conclusions

In this paper, the dynamics of the OH^- + CH_3I reaction has been investigated performing QCT simulations at E_{coll} of 11.5, 23.1, 34.6 and 46.1 kcal mol^{-1} on our high-level *ab initio* PES.[45] Utilizing the explicitly correlated CCSD(T)-F12b method, the stationary points of the proton-abstraction channel have been explored and presented with the previously characterized S_N2 channel.[15] The theoretical analysis for the title reaction has been compared with the revised crossed-beam ion imaging experiments. Briefly, in the case of the branching ratios of the product ions, the internal energy distributions of the S_N2 and proton-abstraction products, as well as the scattering angle distributions of the proton-abstraction products, a pleasant agreement has been found. For proton abstraction, a dominance of the direct stripping mechanism is unveiled, in contrast for S_N2, a rather indirect character is found. The most notable difference between theory and experiment is observed for the scattering angle distributions of CH_3OH at E_{coll} = 23.1 kcal mol^{-1}, where a mixed backward–forward character is measured, while simulations show an isotropic feature. The earlier reported direct dynamics study of Xie *et al.*[14] could not describe the dynamics of the OH^- + CH_3I reaction as accurate as our present QCT simulations, underlining the importance of the accuracy of the PES to provide well comparable results with experiments.

Conflicts of interest

There are no conflicts of interest to declare.

Acknowledgements

The authors at the University of Szeged are thankful for the financial support from the National Research, Development and Innovation Office–NKFIH, Grant No. K-125317; the Ministry of Human Capacities, Hungary, Grant No. 20391-3/2018/FEKUSTRAT; Project No. TKP2021-NVA-19, provided by the Ministry of Innovation and Technology of Hungary from the National Research, Development and Innovation Fund, financed under the TKP2021-NVA funding scheme; the National Young Talent Scholarship (Grant No. NTP-NFTÖ-22-*B*-0050 for D. A. T.); and the Momentum (Lendület) Program of the Hungarian Academy of Sciences. The work at the University of Innsbruck has been supported by the European Research Council (ERC) under the European Union's Horizon 2020 research and innovation programme (grant agreement no. 885479).

References

1 S. S. Shaik, H. B. Schlegel and S. Wolfe, *Theoretical Aspects of Physical Organic Chemistry: The S_N2 Mechanism,* Wiley, New York, 1992.
2 A. H. Maulitz, F. C. Lightstone, Y. J. Zheng and T. C. Bruice, *Proc. Natl. Acad. Sci. U. S. A.*, 1997, **94**, 6591.
3 J. K. Laerdahl and E. Uggerud, *Int. J. Mass Spectrom.*, 2002, **214**, 277.
4 G. Vayner, K. N. Houk, W. L. Jorgensen and J. I. Brauman, *J. Am. Chem. Soc.*, 2004, **126**, 9054.
5 J. M. Gonzales, W. D. Allen and H. F. Schaefer, *J. Phys. Chem. A*, 2005, **109**, 10613.
6 T. A. Hamlin, M. Swart and F. M. Bickelhaupt, *ChemPhysChem*, 2018, **19**, 1315.
7 R. Wester, *Mass Spectrom. Rev.*, 2022, **41**, 627.
8 T. Hansen, P. Vermeeren, L. De Jong, F. M. Bickelhaupt and T. A. Hamlin, *J. Org. Chem.*, 2022, **87**, 8892.
9 X. Lu, C. Shang, L. Li, R. Chen, B. Fu, X. Xu and D. H. Zhang, *Nat. Commun.*, 2022, **13**, 4427.
10 J. D. Evanseck, J. F. Blake and W. L. Jorgensen, *J. Am. Chem. Soc.*, 1987, **109**, 2349.
11 H. Tachikawa, M. Igarashi and T. Ishibashi, *J. Phys. Chem. A*, 2002, **106**, 10977.
12 L. Sun, K. Song and W. L. Hase, *Science*, 2002, **296**, 875.
13 L. Sun, K. Song, W. L. Hase, M. Sena and J. M. Riveros, *Int. J. Mass Spectrom.*, 2003, **227**, 315.
14 J. Xie, R. Sun, M. R. Siebert, R. Otto, R. Wester and W. L. Hase, *J. Phys. Chem. A*, 2013, **117**, 7162.
15 D. A. Tasi, Z. Fábián and G. Czakó, *J. Phys. Chem. A*, 2018, **122**, 5773.
16 H. B. Schlegel, K. Mislow, F. Bernardi and A. Bottoni, *Theor. Chim. Acta*, 1977, **44**, 245.
17 I. Szabó and G. Czakó, *Nat. Commun.*, 2015, **6**, 5972.
18 J. M. Gonzales, R. S. Cox, S. T. Brown, W. D. Allen and H. F. Schaefer, *J. Phys. Chem. A*, 2001, **105**, 11327.
19 J. M. Gonzales, C. Pak, R. Sidney Cox, W. D. Allen, H. F. Schaefer, A. G. Császár and G. Tarczay, *Chem. – Eur. J.*, 2003, **9**, 2173.
20 T. Tsutsumi, Y. Ono, Z. Arai and T. Taketsugu, *J. Chem. Theory Comput.*, 2018, **14**, 4263.
21 T. Tsutsumi, Y. Ono, Z. Arai and T. Taketsugu, *J. Chem. Theory Comput.*, 2020, **16**, 4029.
22 T. Tsutsumi, Y. Ono and T. Taketsugu, *Chem. Commun.*, 2021, **57**, 11734.
23 T. Tsutsumi, Y. Ono and T. Taketsugu, *Top. Curr. Chem.*, 2022, **380**, 19.
24 S. R. Hare, L. A. Bratholm, D. R. Glowacki and B. K. Carpenter, *Chem. Sci.*, 2019, **10**, 9954.
25 Y. G. Proenza, M. A. F. de Souza and R. L. Longo, *Chem. – Eur. J.*, 2016, **22**, 16220.
26 D. A. Tasi and G. Czakó, *Chem. Sci.*, 2021, **12**, 14369.
27 J. Qin, Y. Liu and J. Li, *J. Chem. Phys.*, 2022, **157**, 124301.
28 X. Ji and J. Xie, *Phys. Chem. Chem. Phys.*, 2022, **24**, 7539.
29 A. C. B. De Souza and G. F. Bauerfeldt, *J. Braz. Chem. Soc.*, 2014, **25**, 340.
30 J. Z. A. Laloo, L. Rhyman, O. Larrañaga, P. Ramasami, F. M. Bickelhaupt and A. de Cózar, *Chem. – Asian J.*, 2018, **13**, 1138.
31 S. Zhao, G. Fu, W. Zhen, L. Yang, J. Sun and J. Zhang, *Phys. Chem. Chem. Phys.*, 2022, **24**, 24146.
32 H. Tachikawa and M. Igarashi, *Chem. Phys.*, 2006, **324**, 639.
33 H. Yin, D. Wang and M. Valiev, *J. Phys. Chem. A*, 2011, **115**, 12047.
34 Y. Xu, T. Wang and D. Wang, *J. Chem. Phys.*, 2012, **137**, 184501.
35 J. Chen, Y. Xu and D. Wang, *J. Comput. Chem.*, 2014, **35**, 445.
36 R. Otto, J. Xie, J. Brox, S. Trippel, M. Stei, T. Best, M. R. Siebert, W. L. Hase and R. Wester, *Faraday Discuss.*, 2012, **157**, 41.
37 R. Otto, J. Brox, S. Trippel, M. Stei, T. Best and R. Wester, *Nat. Chem.*, 2012, **4**, 534.
38 J. Xie, S. C. Kohale, W. L. Hase, S. G. Ard, J. J. Melko, N. S. Shuman and A. A. Viggiano, *J. Phys. Chem. A*, 2013, **117**, 14019.
39 J. Xie, R. Otto, R. Wester and W. L. Hase, *J. Chem. Phys.*, 2015, **142**, 244308.
40 J. Xie, J. Zhang and W. L. Hase, *Int. J. Mass Spectrom.*, 2015, **378**, 14.
41 J. Xie, X. Ma, J. Zhang, P. M. Hierl, A. A. Viggiano and W. L. Hase, *Int. J. Mass Spectrom.*, 2017, **418**, 122.
42 J. Xie, J. Zhang, R. Sun, R. Wester and W. L. Hase, *Int. J. Mass Spectrom.*, 2019, **438**, 115.
43 X. Ji, C. Zhao and J. Xie, *Phys. Chem. Chem. Phys.*, 2021, **23**, 6349.
44 J. Xie and W. L. Hase, *Science*, 2016, **352**, 32.
45 D. A. Tasi, T. Győri and G. Czakó, *Phys. Chem. Chem. Phys.*, 2020, **22**, 3775.
46 T. Győri and G. Czakó, *J. Chem. Theory Comput.*, 2020, **16**, 51.
47 C. Møller and M. S. Plesset, *Phys. Rev.*, 1934, **46**, 618.
48 T. B. Adler, G. Knizia and H. J. Werner, *J. Chem. Phys.*, 2007, **127**, 221106.
49 T. H. Dunning, *J. Chem. Phys.*, 1989, **90**, 1007.
50 K. Raghavachari, G. W. Trucks, J. A. Pople and M. Head-Gordon, *Chem. Phys. Lett.*, 1989, **157**, 479.
51 J. Noga and R. J. Bartlett, *J. Chem. Phys.*, 1986, **86**, 7041.
52 M. Kállay and J. Gauss, *J. Chem. Phys.*, 2005, **123**, 214105.
53 K. A. Peterson, D. Figgen, E. Goll, H. Stoll and M. Dolg, *J. Chem. Phys.*, 2003, **119**, 11113.
54 H.-J. Werner, P. J. Knowles, G. Knizia, F. R. Manby and M. Schütz, *et al.*, *Molpro, version 2015.1, a package of ab initio programs*, see **http://www.molpro.net**.
55 M. Kállay, P. R. Nagy, D. Mester, Z. Rolik, G. Samu, J. Csontos, J. Csóka, P. B. Szabó, L. Gyevi-Nagy, B. Hégely, I. Ladjánszki, L. Szegedy, B. Ladóczki, K. Petrov, M. Farkas, P. D. Mezei and Á. Ganyecz, *J. Chem. Phys.*, 2020, **152**, 074107.
56 MRCC, a quantum chemical program suite written by M. Kállay, P. R. Nagy, D. Mester, Z. Rolik, G. Samu,

J. Csontos, J. Csóka, P. B. Szabó, L. Gyevi-Nagy, B. Hégely, I. Ladjánszki, L. Szegedy, B. Ladóczki, K. Petrov, M. Farkas, P. D. Mezei and Á. Ganyecz. See **www.mrcc.hu**.

57 K. A. Brueckner, *Phys. Rev.*, 1954, **96**, 508.

58 W. L. Hase, *Encyclopedia of Computational Chemistry*, Wiley, New York, 1998, pp. 399–407.

59 S. Pratihar, X. Ma, Z. Homayoon, G. L. Barnes and W. L. Hase, *J. Am. Chem. Soc.*, 2017, **139**, 3570.

60 D. A. Tasi and G. Czakó, *J. Chem. Phys.*, 2022, **156**, 184306.

